Letter

Topological nodal point superconductivity in checkerboard magnet-superconductor hybrid systems

Tuan Kieu,[1] Eric Mascot,[2,3] Jasmin Bedow,[1] Roland Wiesendanger,[2] and Dirk K. Morr[1]
[1]*Department of Physics, University of Illinois at Chicago, Chicago, Illinois 60607, USA*
[2]*Department of Physics, University of Hamburg, D-20355 Hamburg, Germany*
[3]*School of Physics, University of Melbourne, Parkville, Victoria 3010, Australia*

(Received 20 January 2023; revised 11 June 2023; accepted 7 July 2023; published 29 August 2023)

We demonstrate that checkerboard magnet-superconductor hybrid (MSH) systems possess a rich phase diagram exhibiting both strong topological superconducting (STSC) and topological nodal point superconducting (TNPSC) phases. We show that TNPSC phases exist both for ferromagnetic and antiferromagnetic systems, yielding a plethora of qualitatively different edge mode structures. Checkerboard MSH systems also facilitate the emergence of STSC phases, which can be induced even in the limit of vanishing magnetization. Our results provide a new path for the quantum engineering of topological superconducting phases using atomic manipulation techniques.

DOI: 10.1103/PhysRevB.108.L060509

Introduction. Magnet-superconductor hybrid (MSH) systems provide a versatile platform for the quantum engineering of topological superconductivity and the ensuing Majorana zero modes. The versatility of MSH systems arises from the fact that their topological phase diagram can be manipulated by changing the MSH system's magnetic structure. Although experimentally, only two-dimensional ferromagnetic (FM) [1–3] and antiferromagnetic (AFM) [4] MSH systems have been realized so far, intriguing topological phase diagrams—involving strong, weak, and higher-order topological superconducting phases—have been theoretically proposed to exist in bicollinear AFM [5], skyrmionic [6], 3**Q** [7], and stacked magnetic structures [8]. Advances in atomic manipulation techniques [9,10] have raised the intriguing possibility to quantum engineer MSH systems [2,11] that interpolate between these various magnetic structures, potentially giving rise to intriguing new topological phase diagrams.

In this Letter, we consider one of these possibilities by studying MSH systems with two sublattices of different magnetic adatoms, yielding a checkerboard magnetic structure [see Fig. 1(a)]. We demonstrate that such systems possess a rich topological phase diagram, exhibiting not only strong topological superconducting (STSC) phases [12,13] characterized by nonzero Chern numbers, but also extended regions of topological nodal point superconductivity (TNPSC) [5, 14–17]. The latter were recently reported to exist in the AFM MSH system Mn/Nb(110) [4], as well as in 4Hb-TaS_2 [18]. We show that TNPSC phases do not only exist in AFM checkerboard systems, but also in FM MSH systems where the chiral symmetry is broken. Moreover, the interplay between the magnetic structure of edges and their real-space direction yields a plethora of qualitatively different edge mode structures. We demonstrate that in checkerboard MSH systems STSC phases can be induced even in the limit of vanishing magnetization, in contrast to uniform FM MSH systems [12,13]. Finally, we show that TNPSC phases can be created using a single species of magnetic adatoms, simplifying their experimental realization. Our results provide a new path to quantum engineer topological superconducting phases using atomic manipulation techniques.

Theoretical Model. To study MSH systems with a magnetic checkerboard structure [see Fig. 1(a)], we consider a two-dimensional superconducting surface and magnetic layer with the same square lattice structure. The two sublattices of the magnetic layer are occupied by different types of magnetic adatoms, and the entire system is described by the Hamiltonian [12,13],

$$\begin{aligned}\mathcal{H} = &-t\sum_{\langle \mathbf{r},\mathbf{r}'\rangle,\sigma} c^\dagger_{\mathbf{r},\sigma}c_{\mathbf{r}',\sigma} - \mu\sum_{\mathbf{r},\sigma} c^\dagger_{\mathbf{r},\sigma}c_{\mathbf{r},\sigma}\\ &+ i\alpha\sum_{\mathbf{r},\boldsymbol{\delta},\sigma,\sigma'} c^\dagger_{\mathbf{r},\sigma}(\boldsymbol{\delta}\times\boldsymbol{\sigma})^z_{\sigma,\sigma'}c_{\mathbf{r}+\boldsymbol{\delta},\sigma'}\\ &- \Delta\sum_{\mathbf{r}}(c^\dagger_{\mathbf{r},\uparrow}c^\dagger_{\mathbf{r},\downarrow} + c_{\mathbf{r},\downarrow}c_{\mathbf{r},\uparrow})\\ &- \sum_{\mathbf{r},\sigma,\sigma'}(J + J_{\mathbf{Q}}e^{i\mathbf{Q}\cdot\mathbf{r}})c^\dagger_{\mathbf{r},\sigma}\mathbf{S}_{\mathbf{r}}\cdot\boldsymbol{\sigma}_{\sigma,\sigma'}c_{\mathbf{r},\sigma'}. \qquad (1)\end{aligned}$$

Here, the operator $c^\dagger_{\mathbf{r},\alpha}$ creates an electron with spin α at site $\mathbf{r}$, $-t$ is the nearest-neighbor hopping amplitude, μ is the chemical potential, α is the Rashba spin-orbit coupling between nearest-neighbor sites $\mathbf{r}$ and $\mathbf{r}+\boldsymbol{\delta}$, and Δ is the s-wave superconducting order parameter. The last term in Eq. (1) describes the coupling between the adatom's spin $\mathbf{S}_{\mathbf{r}}$ of magnitude S at site $\mathbf{r}$ and the conduction electrons with exchange couplings $J \pm J_{\mathbf{Q}}$ in the two sublattices, and $\mathbf{Q} = (\pi,\pi)$ [for details, see the Supplemental Material (SM) [19] Sec.I]. Due to the hard superconducting gap, which suppresses Kondo screening, we can consider the spins of the magnetic adatoms to be classical in nature [20,21]. Below, we consider a somewhat large superconducting order parameter of $\Delta = 0.3t$ in order to ensure a localization length of the edge modes, $\xi_l \sim v_F/\Delta$, which is much smaller than the system size that we can consider numerically. However, the qualitative nature

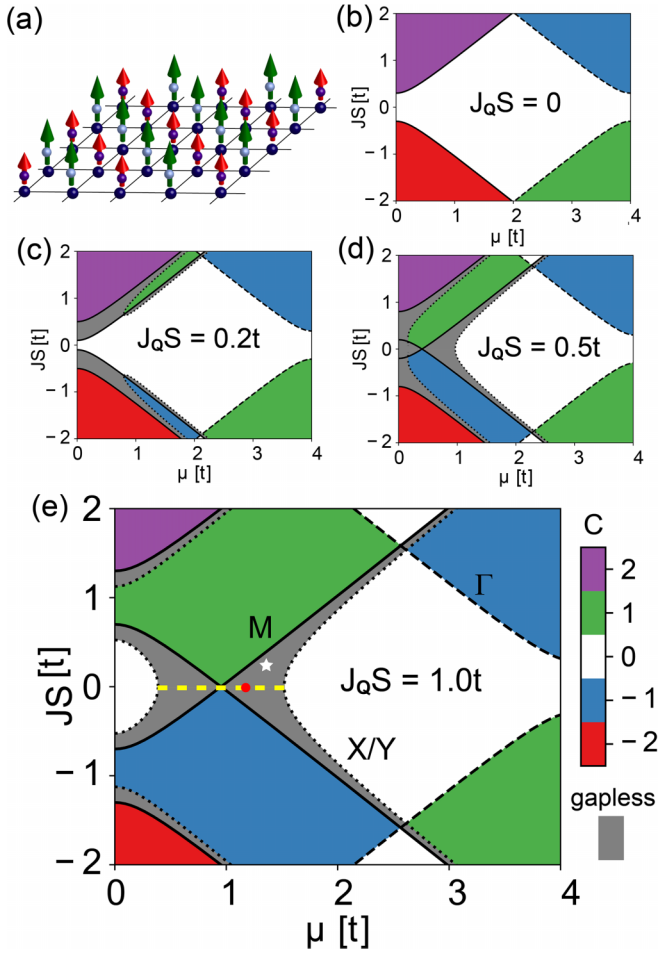

FIG. 1. (a) Schematic of the checkerboard magnetic structure with exchange couplings $J \pm J_{\mathbf{Q}}$ in the two sublattices, as indicated by red and green arrows. (b)-(e) Topological phase diagrams of the MSH system in the (μ, JS) plane for different values of $J_{\mathbf{Q}}S$ with $(\alpha, \Delta) = (0.2, 0.3)t$.

of our results remains unchanged by the particular value of Δ, see the SM [19] Sec. II.

To characterize a strong topological phase, we compute its topological invariant, the Chern number, via [22],

$$C = \frac{1}{2\pi i}\int_{\mathrm{BZ}} d^2k\, \mathrm{Tr}(P_{\mathbf{k}}[\partial_{k_x}P_{\mathbf{k}}, \partial_{k_y}P_{\mathbf{k}}])$$
$$P_{\mathbf{k}} = \sum_{E_n(\mathbf{k})<0} |\Psi_n(\mathbf{k})\rangle\langle\Psi_n(\mathbf{k})|, \qquad (2)$$

where $E_n(\mathbf{k})$ and $|\Psi_n(\mathbf{k})\rangle$ are the eigenenergies and the eigenvectors of the Hamiltonian in Eq. (1) with n being a band index, and the trace is taken over Nambu, spin, and sublattice space. Since STSC phases occur only for $J \neq 0$, they belong to the topological class D [16,23,24].

Finally, for AFM TNPSC phases ($J = 0$), the chiral symmetry of the system allows us to compute a topological charge and characteristic angle associated with nodal points (see the SM [19] Sec. III). We note that trivial nodal point superconductivity was previously discussed in the context of AFM semimetals [25].

Results. We begin by considering the topological phase diagram of the Hamiltonian in Eq. (1), which is presented in Figs. 1(b)–1(e) for different values of $J_{\mathbf{Q}}S$ (the qualitative form of these phase diagrams is independent of the particular values of α and Δ, see the SM [19] Sec. II). For simplicity, we confine our discussion to the $JS \geqslant 0$ part of the phase diagrams. In addition to the strong topological $C = 2, -1$ phases which are already present for $J_{\mathbf{Q}}S = 0$, two new features appear in the phase diagram with increasing $J_{\mathbf{Q}}S$. First, a $C = 1$ phase emerges due to the backfolding of the Brillouin zone (BZ), and the splitting of the bands at the X/Y points. Second, an extended region of the phase diagram (shown in gray), lying between the gap closing lines of the M points (solid black line) and X/Y points (dotted black line), becomes gapless (an analytic expression for the phase transition lines is given in the SM [19] Sec. IV). As one moves in the gapless region between these two gap closing lines, the nodal points move along the magnetic BZ boundary from the M points to the X/Y points. For $J_{\mathbf{Q}}S \geqslant \sqrt{2\alpha^2 + \Delta^2}$, the strong topological $C = \pm 1$ phases touch at a single AFM ($JS = 0$) point in the phase diagram with chemical potential $\mu_c = \sqrt{(J_{\mathbf{Q}}S)^2 - \Delta^2}$. At this point, any nonzero magnetization, which can be induced by arbitrarily small magnetic fields, pushes the system into a STSC phase, in contrast to uniform FM MSH systems, where $JS > \Delta$ is required [12,13] for the emergence of strong topological phases.

To exemplify the electronic structure of an AFM MSH system ($JS = 0$) in the gapless region around μ_c [yellow line in Fig. 1(e)], we consider a system with $\mu = 1.2t$ [red dot in Fig. 1(e)]. In Fig. 2(a), we present the resulting electronic structure exhibiting eight nodal points located along the boundary of the magnetic BZ. Due to the chiral symmetry of the system along the $JS = 0$ line, we find that these nodal points possess a nonzero topological charge $q = \pm 1$ [see Fig. 2(b)], the corresponding characteristic angles are shown in the SM [19] Sec. III. The presence of nodal points with opposite topological charges allows for the emergence of edge modes connecting such nodal points [schematically shown as dashed green lines in Fig. 2(b)] in MSH systems exhibiting edges [5,14–17]. When considering MSH systems in a ribbon geometry possessing diagonal FM or vertical/horizontal AFM edges [see Figs. 2(c) and 2(d)], we find that their electronic structures indeed exhibit such in-gap edge modes as shown by red lines in Figs. 2(e) and 2(f), respectively. However, in contrast to an MSH system with AFM edges, the edge modes along FM edges disperse only weakly around zero energy. To understand this qualitative difference, we note that the projection of the bulk band structure onto momenta parallel to either an FM or AFM edge leads to two overlapping (in momentum space) edge modes [see Fig. 2(b), and the SM [19] Sec. V]. These two edge modes can in general hybridize, and, thus, split in energy. The spectral functions at the FM and AFM edges, shown in the upper and lower panels of Figs. 2(g) and 2(h), respectively, for the two edges of each ribbon, provide insight into the different nature of the resulting edge modes. In contrast to the AFM edge, the edge mode along the FM edge is chiral in nature [13] (due to the broken time-reversal symmetry along the edge) with opposite Fermi velocities on the two FM edges as shown in Fig. 2(g). Thus, the two modes along the FM edges are

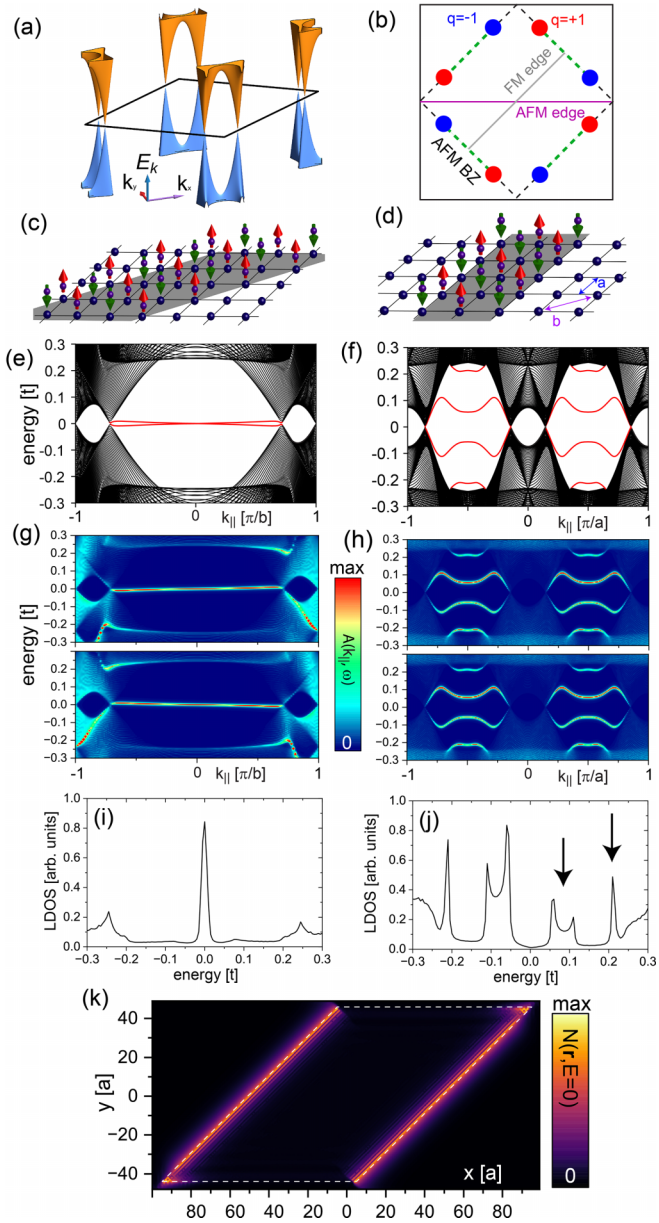

FIG. 2. (a) Energy dispersion of the bulk system in the magnetic BZ. (b) Nodal points and edge modes (dashed green lines) projected onto momenta parallel to the FM and AFM edges. Schematic of (c) diagonal (FM) and (d) vertical (AFM) edges. Electronic structure of a ribbon with (e) FM and (f) AFM edges. (g) and (h) Spectral functions at the ribbon's left (upper panel) and right (lower panel) edges corresponding to (e) and (f). (i) and (j) local density of states (LDOS) at the edges corresponding to (e) and (f). (k) Zero-energy LDOS of a magnetic island (dashed white line) with FM and AFM edges. Parameters are $(\mu, \alpha, \Delta, JS, J_{\mathbf{Q}}S) = (1.2, 0.2, 0.3, 0, 1.0)t$.

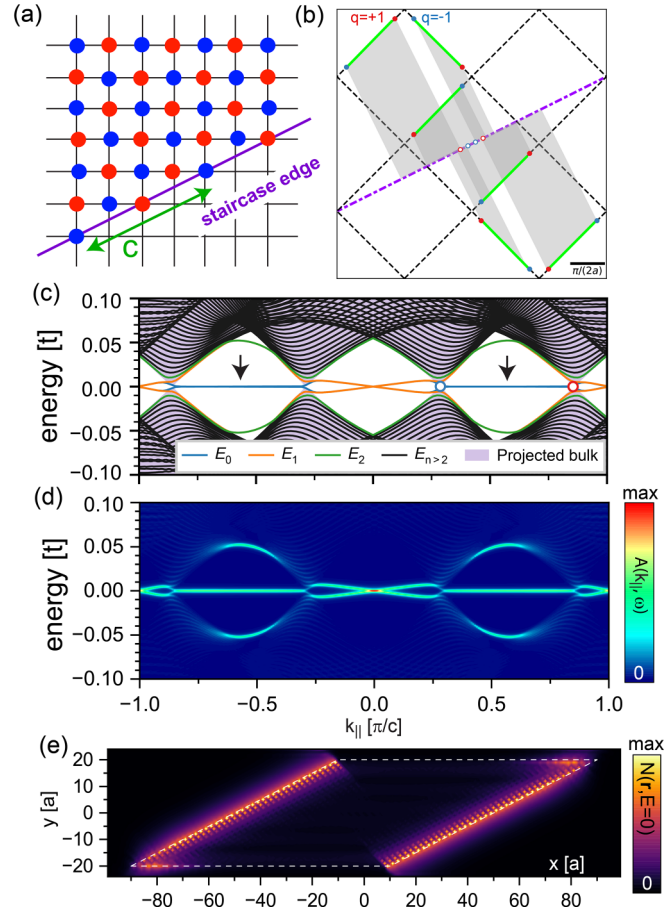

FIG. 3. (a) Schematic of a staircase edge. (b) Projection of edge modes (green lines) connecting nodal points of opposite topological charge onto the momentum axis parallel to the staircase edge (dashed-dotted purple line). Only projected nodes [open blue and red circles] for $-\pi/c \leqslant k_{\parallel} \leqslant \pi/c$ are shown. Dark gray areas represent two overlapping projections. (c) Electronic structure of the ribbon with projected nodal points shown in (b). (d) Edge spectral function. (e) Zero-energy LDOS for a magnetic island with horizontal and staircase edges. Parameters are $(\mu, \alpha, \Delta, JS, J_{\mathbf{Q}}S) = (1.2, 0.2, 0.3, 0, 1.0)t$.

spatially separated, and, thus, do not hybridize. In contrast, the spectral functions at the AFM edges [see Fig. 2(h)] show that both modes exist at the same edge and, thus, strongly hybridize, leading to the much larger energy splitting. This qualitative difference leads to distinct signatures in the LDOS of FM and AFM edges: whereas, the LDOS at an FM edge exhibits a large zero-energy peak [see Fig. 2(i)], the LDOS at the AFM edge exhibits only a low-energy V-like-shaped LDOS [see Fig. 2(j)], with the signatures of the edge modes seen only at higher energies [see black arrows]. As a result, a spatial plot of the zero-energy LDOS of a finite magnetic island [see Fig. 2(k)] reveals large spectral weight along the FM edges and vanishing spectral weight along the AFM edges.

To obtain flat, nondispersive edge modes, it is necessary to consider edges in real space such that the projected edge modes do not completely overlap in momentum space as is the case for the FM and AFM edges (see the SM [19] Sec. V). For example, by considering a staircase-like edge in real space [see Fig. 3(a)], we find that the resulting projection of the nodal points onto momenta parallel to the staircase edge [Fig. 3(b)] yields momentum regions with even and odd numbers of projected modes. In those regions where three projected modes overlap, one edge mode is nondispersive and located at zero energy [see black arrows in Fig. 3(c)], whereas, the other two projected modes hybridize and, thus,

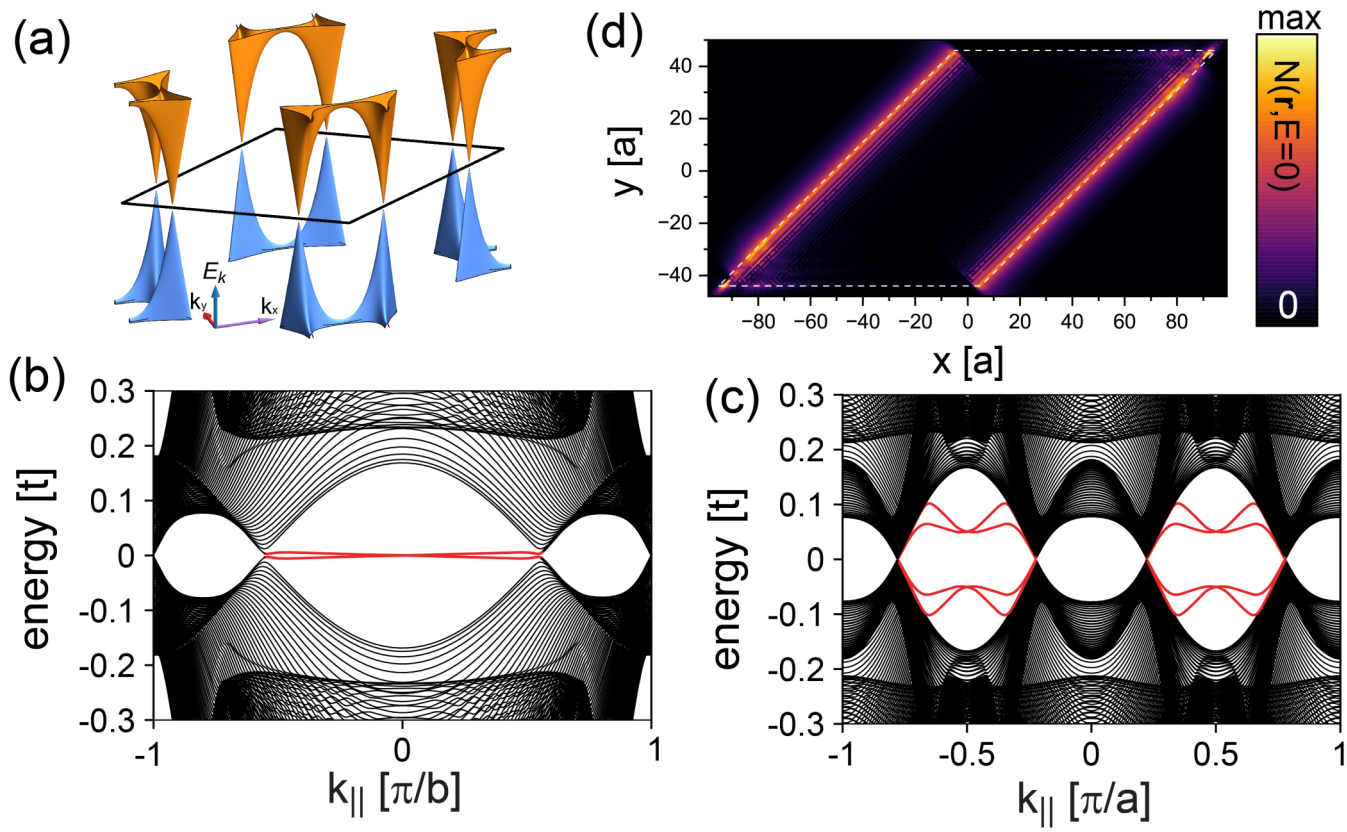

FIG. 4. (a) Energy dispersion of the bulk system in the magnetic BZ. Electronic structure of a ribbon with (b) FM and (c) AFM edges as a function of momentum parallel to the edge. (d) Zero-energy LDOS of a magnetic island (dashed white line) with FM and AFM edges. Parameters are $(\mu, \alpha, \Delta, JS, J_{\mathbf{Q}}S) = (1.4, 0.2, 0.3, 0.25, 1.0)t$.

shift to higher energies. This is also confirmed by a plot of the edge spectral function shown in Fig. 3(d). As a result, a magnetic island that possesses both horizontal and staircase edges [see Fig. 3(e)] again shows a large zero-energy LDOS along the staircase edges, and vanishing spectral weight along the horizontal edges.

The question immediately arises whether the nature of the edge modes persists in those gapless regions of the phase diagram where the chiral symmetry of the AFM is broken due to a nonzero JS. To answer this question, we consider a system in the gapless region above the AFM line as indicated by a white star in Fig. 1(e). The bulk electronic structure of this system again reveals eight nodal points along the magnetic BZ boundary as shown in Fig. 4(a). The electronic dispersions for ribbons with FM and AFM edges [Figs. 4(b) and 4(c), respectively] reveal the same qualitative nature of the respective edge modes as in the $JS = 0$ case discussed in Fig. 2. However, since the chiral symmetry of the AFM edge is broken due to the nonzero JS, the double-degeneracy of the AFM edge modes is lifted, leading to a further energy splitting among them. The zero-energy LDOS of a magnetic island [see Fig. 4(d)], thus, again reveals large spectral weight along the FM edges and vanishing spectral weight along the AFM edges. Since similar results are obtained not only for any point in the gapless regions around μ_c [see Fig. 1(e)], but also in the gapless regions induced by much smaller values of $J_{\mathbf{Q}}S$ [see Figs. 1(c) and 1(d)], we conclude that checkerboard MSH systems are ideally suited to quantum engineer topological nodal point superconductivity as the occurrence of TNPSC phases does not require the fine-tuning of parameters. Of particular interest here are MSH systems with large Rashba spin-orbit coupling since the extent of gapless regions in the phase diagram increases with α (see the SM [19] Sec. II). Our findings provide further support for the conclusion of recent scanning tunneling spectroscopy (STS) experiments [4] that the presence or absence of (near) zero-energy edge modes at various edges in the AFM MSH system Mn/Nb(110) are characteristic signatures of the underlying TNPSC phase.

A special case of the magnetic checkerboard structure arises when $J = J_{\mathbf{Q}}$, implying that only a single species of magnetic adatoms is present in one of the two sublattices as schematically shown in Fig. 5(a). In Fig. 5(b), we present the resulting phase diagram. In addition to the strong topological $C = 1$ phase, we obtain three types of gapless regions. Region 1 is entered from the gapped trivial ($C = 0$) region via a gap closing at the X/Y points. As a result, the edge modes connect the nodal points of opposite topological charge that are located on the same edge of the magnetic BZ. In this region, the electronic structure along FM and AFM edges [see Figs. 5(c) and 5(d)] is similar to that shown in Fig. 2. In contrast, the transition into region 2 from the trivial phase requires a gap closing at the M points, which yields edge modes connecting the nodal points of opposite topological charge on neighboring edges of the magnetic BZ [see Figs. 5(e) and 5(f)]. In this case, neither edge shows a (nearly) nondispersive edge mode, implying the absence of any pronounced zero-energy peak in

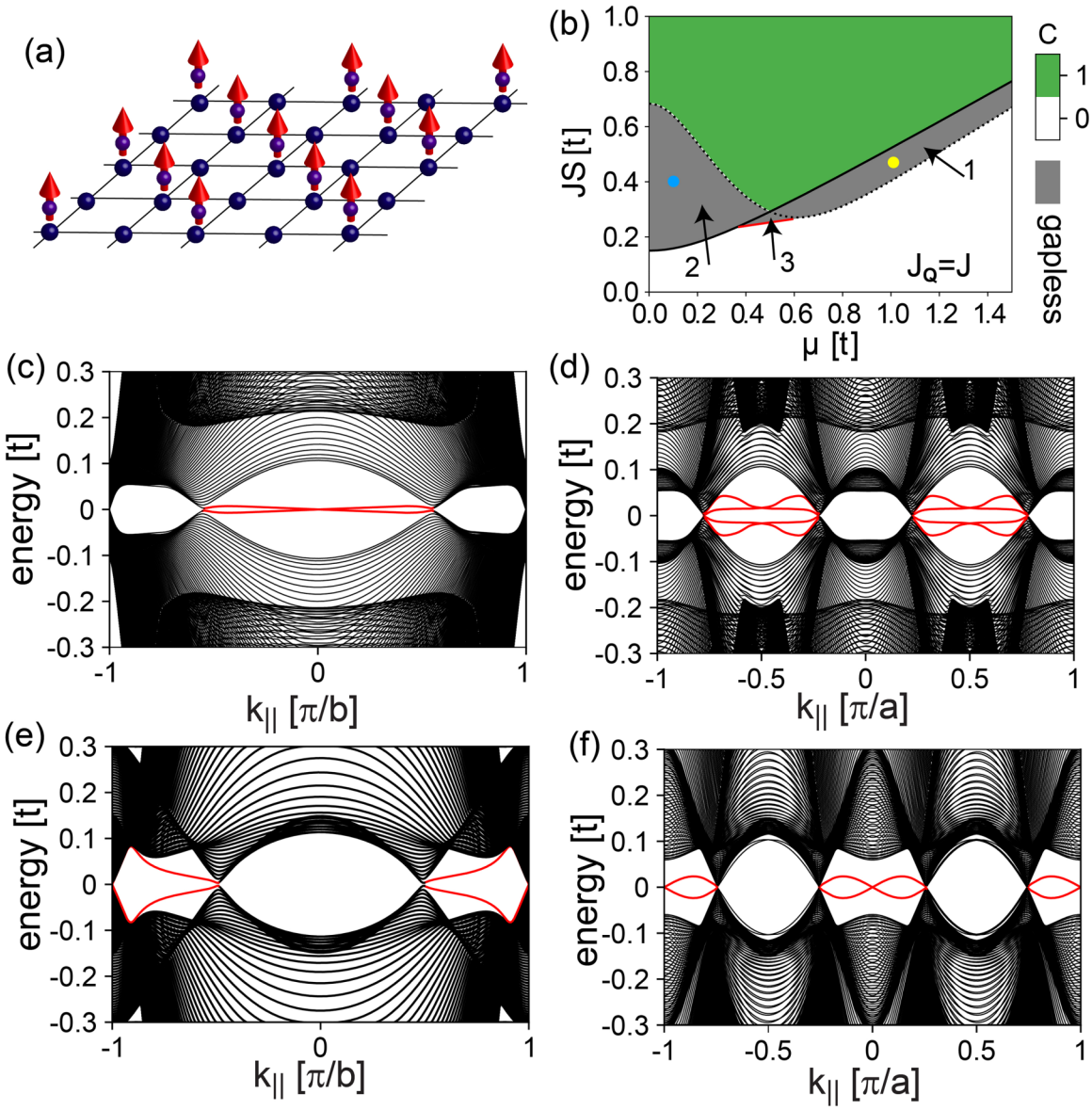

FIG. 5. (a) Schematic of the checkerboard magnetic structure for $J = J_Q$. (b) Topological phase diagram for $(\alpha, \Delta) = (0.2, 0.3)t$. Electronic structure of an MSH ribbon with (c) and (e) FM and (d) and (f) AFM edges for $(\mu, JS) = (1.0, 0.47)t$ [yellow dot in (b)], and $(\mu, JS) = (0.1, 0.4)t$ [blue dot in (b)], respectively.

the LDOS at the edges. Finally, the transition line into region 3 (red line) shows gap closings that vary along the magnetic BZ boundary between the M points and the X/Y points. We, thus, conclude that by using a single species of magnetic adatoms, it is possible to create a TNPSC phase.

Discussion. We have shown that checkerboard MSH systems are ideally suited to quantum engineer STSC as well as TNPSC phases with the latter existing both for AFM ($J = 0$) and FM ($J \neq 0$) structures. The nature of edge modes in the TNPSC phases is determined by the projection of nodal points onto the edge momenta and the magnetic structure of the edge. This allows for the emergence of edge modes that are dispersive in some momentum ranges and nondispersive (flat) in others. Our results further support the conclusions of recent STS experiments in the AFM MSH system Mn/Nb(110) [4] that the underlying TNPSC phase can be identified through the presence or absence of (near) zero-energy edge modes along different edges in the system. The finding that TNPSC can be created in checkerboard MSH systems where the chiral symmetry is broken, such as the ones discussed in Figs. 4 and 5, and that the characteristic dependence of edge modes on the edge structure persists, opens new classes of materials for the exploration of TNPSC. Advances in atomic manipulation techniques all but ensure that such checkerboard MSH systems and the ensuing TNPSC phases can be quantum engineered in the near future.

Acknowledgments. We would like to thank S. Rachel for stimulating discussions. T.K, E.M., J.B., and D.K.M. acknowledge support by the U.S. Department of Energy, Office of Science, Basic Energy Sciences, under Award No. DE-FG02-05ER46225. R.W. acknowledges financial support by

the EU via the ERC Advanced Grant ADMIRE (No. 786020) and the Deutsche Forschungsgemeinschaft via the Cluster of Excellence "Advanced Imaging of Matter" (EXC 2056, Project ID No. 390715994).

[1] G. C. Ménard, S. Guissart, C. Brun, R. T. Leriche, M. Trif, F. Debontridder, D. Demaille, D. Roditchev, P. Simon, and T. Cren, Two-dimensional topological superconductivity in Pb/Co/Si(111), Nat. Commun. **8**, 2040 (2017).

[2] A. Palacio-Morales, E. Mascot, S. Cocklin, H. Kim, S. Rachel, D. K. Morr, and R. Wiesendanger, Atomic-scale interface engineering of Majorana edge modes in a 2D magnet-superconductor hybrid system, Sci. Adv. **5**, eaav6600 (2019).

[3] S. Kezilebieke, M. N. Huda, V. Vaňo, M. Aapro, S. C. Ganguli, O. J. Silveira, S. Głodzik, A. S. Foster, T. Ojanen, and P. Liljeroth, Topological superconductivity in a van der Waals heterostructure, Nature (London) **588**, 424 (2020).

[4] M. Bazarnik, R. Lo Conte, E. Mascot, K. Von Bergmann, D. K. Morr, and R. Wiesendanger, Antiferromagnetism-driven two-dimensional topological nodal-point superconductivity, Nat. Commun. **14**, 614 (2023).

[5] R.-X. Zhang, W. S. Cole, X. Wu, and S. Das Sarma, Higher-Order Topology and Nodal Topological Superconductivity in Fe(Se,Te) Heterostructures, Phys. Rev. Lett. **123**, 167001 (2019).

[6] E. Mascot, J. Bedow, M. Graham, S. Rachel, and D. K. Morr, Topological superconductivity in skyrmion lattices, npj Quantum Mater. **6**, 6 (2021).

[7] J. Bedow, E. Mascot, T. Posske, G. S. Uhrig, R. Wiesendanger, S. Rachel, and D. K. Morr, Topological superconductivity induced by a triple- **q** magnetic structure, Phys. Rev. B **102**, 180504(R) (2020).

[8] K. H. Wong, M. R. Hirsbrunner, J. Gliozzi, A. Malik, B. Bradlyn, T. L. Hughes, and D. K. Morr, Higher order topological superconductivity in magnet-superconductor hybrid systems, npj Quantum Mater. **8**, 31 (2023).

[9] K. K. Gomes, W. Mar, W. Ko, F. Guinea, and H. C. Manoharan, Designer Dirac fermions and topological phases in molecular graphene, Nature (London) **483**, 306 (2012).

[10] M. Polini, F. Guinea, M. Lewenstein, H. C. Manoharan, and V. Pellegrini, Artificial honeycomb lattices for electrons, atoms and photons, Nat. Nanotechnol. **8**, 625 (2013).

[11] H. Kim, A. Palacio-Morales, T. Posske, L. Rózsa, K. Palotás, L. Szunyogh, M. Thorwart, and R. Wiesendanger, Toward tailoring Majorana bound states in artificially constructed magnetic atom chains on elemental superconductors, Sci. Adv. **4**, eaar5251 (2018).

[12] J. Li, T. Neupert, Z. Wang, A. H. MacDonald, A. Yazdani, and B. A. Bernevig, Two-dimensional chiral topological superconductivity in Shiba lattices, Nat. Commun. **7**, 12297 (2016).

[13] S. Rachel, E. Mascot, S. Cocklin, M. Vojta, and D. K. Morr, Quantized charge transport in chiral Majorana edge modes, Phys. Rev. B **96**, 205131 (2017).

[14] Y. Baum, T. Posske, I. C. Fulga, B. Trauzettel, and A. Stern, Gapless topological superconductors: Model Hamiltonian and realization, Phys. Rev. B **92**, 045128 (2015).

[15] J.-T. Kao, S.-M. Huang, C.-Y. Mou, and C. C. Tsuei, Tunneling spectroscopy and Majorana modes emergent from topological gapless phases in high- T c cuprate superconductors, Phys. Rev. B **91**, 134501 (2015).

[16] C.-K. Chiu, J. C. Y. Teo, A. P. Schnyder, and S. Ryu, Classification of topological quantum matter with symmetries, Rev. Mod. Phys. **88**, 035005 (2016).

[17] W.-Y. He, B. T. Zhou, J. J. He, N. F. Q. Yuan, T. Zhang, and K. T. Law, Magnetic field driven nodal topological superconductivity in monolayer transition metal dichalcogenides, Commun. Phys. **1**, 40 (2018).

[18] A. K. Nayak, A. Steinbok, Y. Roet, J. Koo, G. Margalit, I. Feldman, A. Almoalem, A. Kanigel, G. A. Fiete, B. Yan, Y. Oreg, N. Avraham, and H. Beidenkopf, Evidence of topological boundary modes with topological nodal-point superconductivity, Nat. Phys. **17**, 1413 (2021).

[19] See Supplemental Material at http://link.aps.org/supplemental/10.1103/PhysRevB.108.L060509 for further support of the conclusions and results presented in the main text.

[20] A. V. Balatsky, I. Vekhter, and J.-X. Zhu, Impurity-induced states in conventional and unconventional superconductors, Rev. Mod. Phys. **78**, 373 (2006).

[21] B. W. Heinrich, J. I. Pascual, and K. J. Franke, Single magnetic adsorbates on s -Wave superconductors, Prog. Surf. Sci. **93**, 1 (2018).

[22] J. E. Avron, R. Seiler, and B. Simon, Homotopy and Quantization in Condensed Matter Physics, Phys. Rev. Lett. **51**, 51 (1983).

[23] A. Kitaev, in *Advances in Theoretical Physics: Landau Memorial Conference*, AIP Conf. Proc. No. 1134 (AIP, Melville, NY, 2009), p. 22.

[24] S. Ryu, A. P. Schnyder, A. Furusaki, and A. W. W. Ludwig, Topological insulators and superconductors: Tenfold way and dimensional hierarchy, New J. Phys. **12**, 065010 (2010).

[25] W. Brzezicki and M. Cuoco, Nodal s -Wave superconductivity in antiferromagnetic semimetals, Phys. Rev. B **97**, 064513 (2018).